

Article

Decomposition Characteristics of SF₆ and Partial Discharge Recognition under Negative DC Conditions

Ju Tang ¹, Xu Yang ¹, Gaoxiang Ye ¹, Qiang Yao ², Yulong Miao ² and Fuping Zeng ^{1,*}

¹ School of Electrical Engineering, Wuhan University, Wuhan 430072, China; whtangju@whu.edu.cn (J.T.); 15102738342@126.com (X.Y.); 2015202070095@whu.edu.cn (G.Y.)

² Chongqing Electric Power Research Institute, Chongqing Power Company, Chongqing 401123, China; 2012202070085@whu.edu.cn (Q.Y.); ygxflyhigh@163.com (Y.M.)

* Correspondence: Fuping.Zeng@whu.edu.cn; Tel.: +86-027-6877-2323

Academic Editor: Issouf Fofana

Received: 17 March 2017; Accepted: 17 April 2017; Published: 18 April 2017

Abstract: Four typical types of artificial defects are designed in conducting the decomposition experiments of SF₆ gas to obtain and understand the decomposition characteristics of SF₆ gas-insulated medium under different types of negative DC partial discharge (DC-PD), and use the obtained decomposition characteristics of SF₆ in diagnosing the type and severity of insulation fault in DC SF₆ gas-insulated equipment. Experimental results show that the negative DC partial discharges caused by the four defects decompose the SF₆ gas and generate five stable decomposed components, namely, CF₄, CO₂, SO₂F₂, SOF₂, and SO₂. The concentration, effective formation rate, and concentration ratio of SF₆ decomposed components can be associated with the PD types. Furthermore, back propagation neural network algorithm is used to recognize the PD types. The recognition results show that compared with the concentrations of SF₆ decomposed components, their concentration ratios are more suitable as the characteristic quantities for PD recognition, and using those concentration ratios in recognizing the PD types can obtain a good effect.

Keywords: SF₆; negative DC-PD; decomposed components; concentration ratio; back propagation neural network; PD recognition

1. Introduction

Given the connection of new large-scale energy and the rapid development of HVDC transmission technology and flexible HVDC technology, DC gas-insulated equipment (DC-GIE) has attracted significant attention because of its technological advantages in improving system reliability and reducing space occupation [1–6]. Pure SF₆ gas has stable chemical properties and is not easily decomposed. However, under the effect of the partial discharge (PD), spark discharge, arc discharge, overheating, and other factors, SF₆ gas is decomposed into various low-fluoride sulfides (such as SF₅, SF₄, SF₃, SF₂, and SF). These low-fluoride sulfides then react with the trace air and moisture that inevitably exist in the DC-GIE to produce stable decomposition products, such as sulfuranyl fluoride (SO₂F₂), thionyl fluoride (SOF₂), thionyl tetrafluoride (SOF₄), sulfur dioxide (SO₂), carbon tetrafluoride (CF₄), carbon dioxide (CO₂), hydrogen fluoride (HF), and hydrogen sulfide (H₂S) [7–12]. Some of these products, particularly SO₂, HF, and H₂S, can corrode metal parts and solid insulation in equipment, thereby accelerating insulation aging and reducing the overall insulation performance of the equipment. Eventually, the safe and reliable operation of the equipment and the entire power grid is compromised.

SF₆ gas component analysis (GCA) is a non-electrical detection method, which can effectively avoid the complex electromagnetic interference of substations and has become a popular research

topic in recent years [13–16]. In [17–19], the SF₆ decomposed products under arc, spark, and corona discharges were studied. Tang et al. compared and analyzed the decomposition characteristics of SF₆ under two types of common PDs [20], and recognized four typical PD types [21,22]. A large number of studies have shown that the type, concentration, and formation law of SF₆ decomposed components are closely related to the type and severity of insulation faults in GIE. However, the recent studies have mainly focused on monitoring the insulation status of AC-GIE using the decomposition characteristics of SF₆ under PD [23–28]. The research focus has not extended to the DC field yet.

Therefore, four artificial models are designed in this study to simulate the common insulation defects in DC-GIE. These four defect models are placed in the built decomposition device of SF₆ under negative DC conditions, respectively, and PD initial voltage is applied 1.2 times on the defect. As a result, SF₆ decomposes differently under the four defects, and the decomposed components are quantitatively detected by the gas chromatography/mass spectrometry (GC/MS) detection method. The decomposition characteristics of SF₆ under four types of negative DC partial discharge (DC-PD) are obtained. The relationship between the decomposition characteristics of SF₆ and the PD types was further studied. Moreover, back propagation (BP) neural network algorithm [29–38] is used to recognize the PD types. Then, the best characteristic quantity for PD recognition is extracted. This study lays a solid foundation of using GCA method to diagnose the insulation faults in DC-GIE and assess its insulation status.

2. Experiment

2.1. Experimental Wiring

The experimental wiring of SF₆ decomposition under negative DC-PD is illustrated in Figure 1. A voltage regulator (T_1 : 0–380 V) and a testing transformer (T_2 : 50 kVA/100 kV) provide the AC high voltage (AC-HV). The AC-HV is converted into DC testing voltage by using a half-wave rectifier circuit, which comprises a HV silicon stack (D_s : 100 kV/5 A) and a filter capacitor (C_f : 0.2 μ F). Two protective resistors (R_1 : 20 k Ω , R_2 : 20 k Ω) are used to protect the system. A capacitive voltage divider (C_v) is used to measure the value of AC output voltage of the transformer, and a resistive voltage divider (R_v) is employed to measure the value of DC testing voltage applied across the defect. A coupling capacitor (C_k : 500 pF/100 kV) is used to extract the pulse voltage. A non-inductive detection impedance (Z_m : 50 Ω) is used to send the pulse current signal to the digital storage oscilloscope (DSO). The DSO (WavePro 7100XL, New York, USA, analogue band: 1 GHz, sampling rate: 20 GHz, memory depth: 48 MB) is used to monitor the PD magnitude. The structure of the gas chamber is shown in Figure 2, and its volume is 60 L. A GC/MS (Shimadzu QP-2010Ultra, Kyoto, Japan, precision: 0.01 ppm, accuracy: $\pm 10\%$) is used to measure the sample gas components quantitatively. The GC/MS uses He (purity: 99.9995%) as the carrier gas and deploys the special capillary column CP-Si15CB (Shimadzu, Kyoto, Japan) to separate different components.

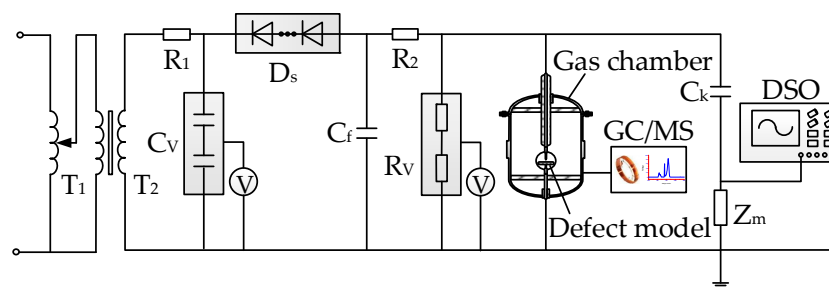


Figure 1. Experimental wiring of SF₆ decomposition under negative DC-PD.

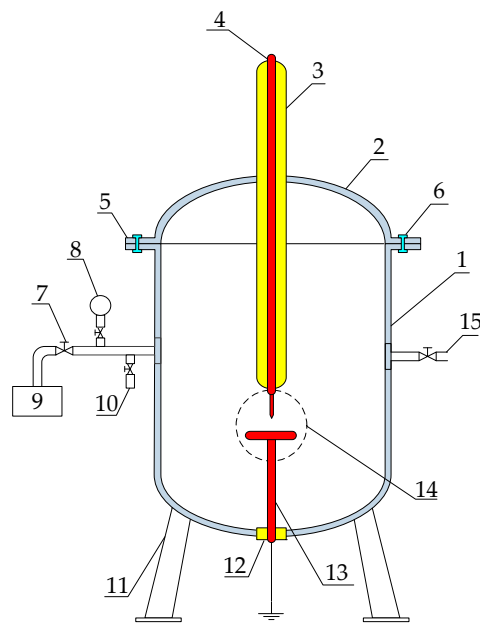


Figure 2. Structure of the gas chamber: 1 stainless-steel shell; 2 top cover; 3 HV bushing; 4 HV conductor; 5 flange; 6 screw; 7 ball valve; 8 vacuum pressure gauge; 9 vacuum pump; 10 injection port; 11 supporting foot; 12 epoxy loop; 13 ground conductor; 14 insulation defect; and 15 sampling port.

2.2. Insulation Defect Model

As shown in Figure 3, typical defects in practical DC-GIE include: metallic protrusion, which is usually manifested as the abnormal bulge on a HV conductor [39]; free conductive particle, which is generally shown as the metal powder that can move freely in a cavity [40]; insulator pollution, which is formed by various pollution on the surface of an insulator [41]; and insulator gap, which is formed by peeling a gap between a HV conductor and disc insulator [42]. The protrusion defect is the most harmful and the particle defect is the most typical in DC-GIE. According to the characteristics of these defects, the four defect models (protrusion defect, particle defect, pollution defect, and gap defect) are designed in this study for experimental research, as shown in Figure 4. All electrodes shown in Figure 4 are made of stainless steel, and all plate electrodes have the same size: the thickness and diameter are 10 mm and 120 mm, respectively. The experiment in this study uses a needle-plate model to simulate the protrusion defect (Figure 4a). The distance between the needle and the plate is 10 mm. The curvature radius of the needle tip is 0.3 mm. The model of the particle defect consists of a ball electrode (HV electrode), a bowl electrode (ground electrode), and 20 aluminum balls (Figure 4b).

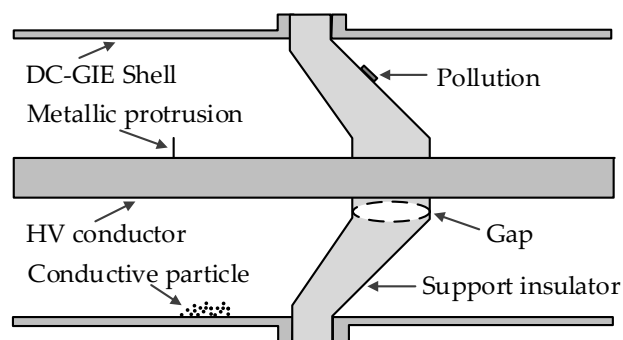


Figure 3. Typical defects in DC-GIE.

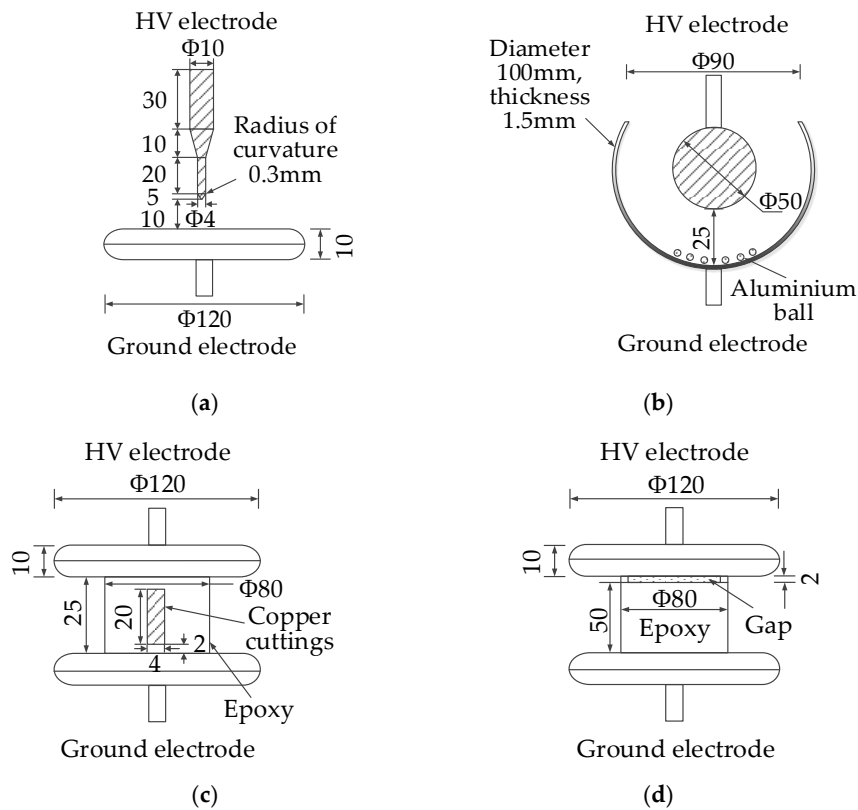


Figure 4. Four kinds of insulation defect models (Unit: mm): (a) Protrusion defect; (b) Particle defect; (c) Pollution defect; and (d) Gap defect.

The diameter of the ball electrode is 50 mm. A hollow sphere is cut to obtain the bowl electrode. The diameters of the hollow sphere, circular incision, and aluminum ball are 100 mm, 90 mm, and 3 mm, respectively. The ball and bowl electrodes form a concentric sphere structure. Some copper cuttings are adhered on the surface of an epoxy cylinder to simulate the pollution defect (Figure 4c). The epoxy is inserted between two plate electrodes. The size of the copper cuttings is 4 mm × 20 mm. The epoxy cylinder is 25 mm thick and 80 mm in diameter. An epoxy cylinder is inserted between the two plate electrodes to create the gap defect model (Figure 4d). A 2-mm gap is maintained between the HV electrode and the epoxy. The epoxy cylinder is 50 mm thick and 80 mm in diameter.

2.3. Experimental Method

The experimental system is connected as shown in Figure 1. The defect model is placed in the gas chamber, which is cleaned three times with SF₆ gas. Then, the chamber is filled with 0.2 MPa SF₆. The concentration of H₂O and O₂ in the chamber satisfy the industrial standard of DL/T 596-1996 [43]. The experimental voltage is raised gradually until the oscilloscope can detect the PD signal. This voltage is the PD initial voltage (U_0). The decomposition experiment of SF₆ is conducted for 96 h under the voltage of 1.2 U_0 . The SF₆ decomposed components are collected every 12 h. GC/MS is used to measure the component concentration. All the experiments are conducted under the same conditions to ensure comparability. The laboratory temperature and relative humidity are maintained at 20 °C and 50%, respectively. The purity of SF₆ gas is 99.9995%.

The experimental results show that the PD initial voltage of the system without the defect is 82 kV. The PD initial voltages of the system after placing the four defects, and the corresponding experimental voltages are shown in Table 1. No breakdown occurred at each experimental voltage.

Table 1. Experimental voltages under four kinds of defects.

Voltage	Defect Type			
	Protrusion	Particle	Pollution	Gap
PD initial voltage (U_0)	−31.2 kV	−28.3 kV	−20.3 kV	−49.7 kV
Experimental voltage ($1.2 U_0$)	−37.4 kV	−34.0 kV	−24.4 kV	−59.6 kV

3. Experimental Results

3.1. PD Characteristics

PD has a cumulative effect on SF₆ decomposition. That is, PD repetition rate (N , unit: pulse/s), the average discharge magnitude of a single pulse (Q_{avg} , unit: pC/pulse), and the average discharge magnitude in a second (Q_{sec} , unit: pC/s) affect the SF₆ decomposition. A certain relationship exists among these three parameters (N , Q_{avg} , and Q_{sec}), as shown in Equation (1). The measurements of N , Q_{avg} , and Q_{sec} under the four defects are shown in Table 2. This experiment uses a 50 Ω non-inductive resistor pulse detection unit to monitor the PD waveforms. A PD calibration circuit is used to calibrate the PD magnitude, as recommended by IEC 60270:2000 [44]:

$$Q_{sec} = Q_{avg} \times N \quad (1)$$

Table 2. N , Q_{avg} , and Q_{sec} of PD caused by four kinds of defects.

Defect Type	N (pulse/s)	Q_{avg} (pC/pulse)	Q_{sec} (pC/s)
Protrusion	1836	3.9	7160.4
Particle	322	10.5	3381.0
Pollution	216	6.1	1317.6
Gap	18	29.1	523.8

Table 2 shows that the PD characteristics under the four defects are significantly different. Under the protrusion defect, Q_{avg} is the smallest, N and Q_{sec} are the largest, and discharge is the most stable. In this study, the aluminum balls are selected as the metal particles that can move freely. The aluminum balls easily jump under the influence of an electric field. After the aluminum balls fall, they slide to the bottom of the bowl electrode. These balls have a concentrated distribution while moving. Therefore, the PD under the particle defect is stable. Moreover, the PD has the second largest N , Q_{avg} , and Q_{sec} under the particle defect compared with those under the other three defects. Under the pollution defect, Q_{avg} and Q_{sec} are small, and N is slightly smaller than that under the particle defect. Under the same experimental conditions, the gap defect has the most difficulty in producing PD, under this defect, Q_{avg} is the largest, N and Q_{sec} are the smallest, and discharge has a large dispersion. In summary, the N , Q_{avg} , and Q_{sec} under the four defects are significantly different, which is the basic reason for the difference in the SF₆ decomposition. This result provides a possibility to study and establish the corresponding relationship between the decomposition characteristics of SF₆ and the defect types.

3.2. Concentrations of SF₆ Decomposed Components

Experimental results show that the negative DC partial discharges caused by the four defects decompose SF₆ gas and generate five stable decomposed components, namely, CF₄, CO₂, SO₂F₂, SOF₂, and SO₂. The relationship between these five decomposed components and the defect types is investigated in this study.

3.2.1. Concentrations of CF₄ and CO₂

As shown in Figure 5a, the CF₄ concentration presents a “linearly saturated” growth trend with time under the particle defect. Under the protrusion and pollution defects, the CF₄ concentrations present an approximately linear growth trend with time. Under the gap defect, the CF₄ concentration features the popular logistic population growth trend called the “S” growth trend with time [45,46]. At 96 h, the CF₄ concentration is 2.37 ppm under the particle defect. The CF₄ concentrations are less than 0.32 ppm under the other three defects. Thus, the generation amounts of CF₄ are small, and the change curves of the CF₄ concentrations under these three defects are close to one another and have two intersections in 24 h. Errors existed when GC/MS is used to detect the gas concentration. Therefore, this study does not recommend selecting CF₄ concentration as a characteristic quantity to recognize the PD types. However, CF₄ concentration can be used as an auxiliary criterion for identifying the particle defect.

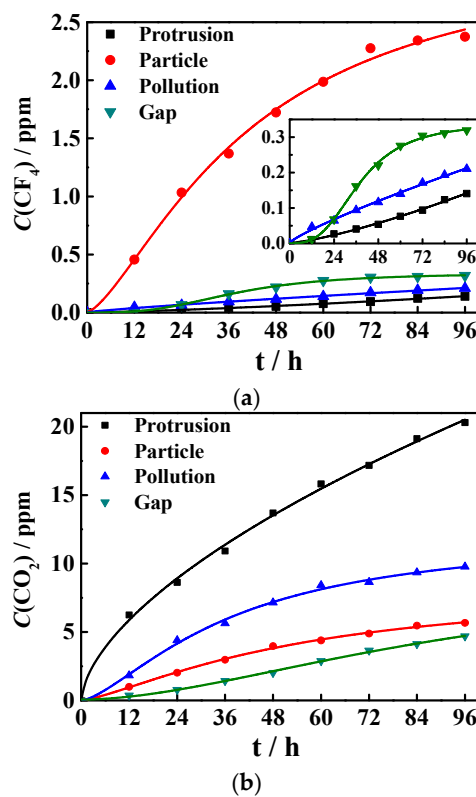


Figure 5. Change curves of the concentrations of CF₄ and CO₂ with time: (a) CF₄; and (b) CO₂.

As shown in Figure 5b, the CO₂ concentration presents an approximately linear growth trend with time under the gap defect. Under the other three defects, the CO₂ concentrations present a “linearly saturated” growth trend with time. At 96 h, the concentration relationship of CO₂ under the four defects is as follows: protrusion defect (20.3 ppm) > pollution defect (9.77 ppm) > particle defect (5.67 ppm) > gap defect (4.69 ppm). CO₂ is generated by the reaction of C atoms and O₂. Under the effect of the electric field, the charged particles hit the surface of the electrodes and release C atoms. During the experiment, the applied voltage remains constant, and C atoms are produced continually. Therefore, the growth trend of CO₂ is mainly determined by the O₂ concentration in the chamber. In the early stage of the experiment, O₂ is abundant, thus, the CO₂ concentrations increase linearly with time under the four defects. Under the gap defect, the N and Q_{sec} are small, and the generation amounts of SF₆ decomposed components are small. Hence, the consumed O₂ concentration is also small. In the late stage of the experiment, O₂ is also abundant, thus, the CO₂ concentration increases linearly with

time under the gap defect. Compared with those under the gap defect, the generation amounts of SF_6 decomposed components under the other three defects are significantly larger, thus, the consumed O_2 concentrations are also remarkably larger. In the late stage of the experiment, the remaining small amount of O_2 inhibits the CO_2 formation to some extent, thus, the CO_2 concentrations present a saturated growth trend with time under the other three defects. According to the growth trend and the value of CO_2 concentration, the four defects can be distinguished from one another. Therefore, CO_2 concentration can be selected as a characteristic quantity to recognize the PD types.

3.2.2. Concentrations of SO_2F_2 , SOF_2 , and SO_2

Under the four defects, the concentrations of SO_2F_2 , SOF_2 , and SO_2 approximately present a “linearly saturated” growth trend with time (Figure 6).

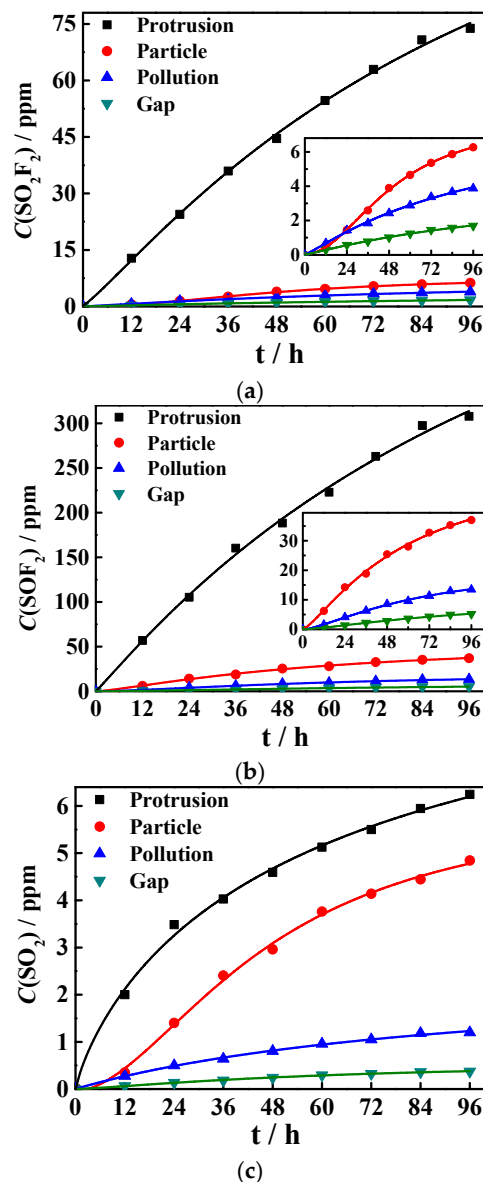


Figure 6. Change curves of the concentrations of SO_2F_2 , SOF_2 , and SO_2 with time: (a) SO_2F_2 ; (b) SOF_2 ; and (c) SO_2 .

The concentration relationships of SO_2F_2 , SOF_2 , and SO_2 under the four defects are the same, namely, protrusion defect > particle defect > pollution defect > gap defect, which are consistent with

the value relationships of N and Q_{sec} under the four defects. Thus, the N and Q_{sec} of PD are the main factors that influence the formations of SO_2F_2 , SOF_2 , and SO_2 . The differences among the curves in Figure 6a,b are evident. According to the growth trend and the value of SO_2 concentration, the four defects can be distinguished from one another. Therefore, the concentrations of SO_2F_2 , SOF_2 , and SO_2 can be selected as characteristic quantities to recognize the PD types.

The formation processes of SO_2F_2 and SOF_2 are shown in Figure 7. Under the effect of the electric field, the charged particles hit the SF_6 molecule and generate low-fluoride sulfides (such as SF_5 , SF_4 , SF_3 , and SF_2), and hit the H_2O and O_2 molecules and generate O atom and OH ion. During the experiment, the applied voltage remains constant, and low-fluoride sulfides are produced continually. Therefore, the growth trends of SO_2F_2 and SOF_2 are mainly determined by the concentrations of H_2O and O_2 in the chamber. In the early stage of the experiment, H_2O and O_2 are abundant, thus, the concentrations of SO_2F_2 and SOF_2 increase linearly with time. H_2O and O_2 in the chamber are gradually consumed with time. Moreover, the formation rates of SO_2F_2 and SOF_2 are significantly larger than other components. In the late stage of the experiment, the further increase in the concentrations of SO_2F_2 and SOF_2 at large rates is difficult to ensure with the remaining H_2O and O_2 in the chamber, thus the formations of SO_2F_2 and SOF_2 are prevented to some extent. Therefore, the concentrations of SO_2F_2 and SOF_2 present a saturated growth trend with time in the late stage of the experiment.

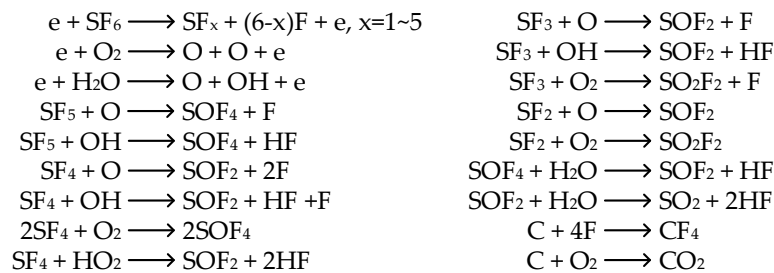


Figure 7. Formation process of SF_6 decomposed components.

SO_2 is produced by the hydrolysis reaction of SOF_2 . Thus, the growth trend of SO_2 is determined by the concentrations of SOF_2 and H_2O . The SOF_2 concentrations present a “linearly saturated” growth trend with time under the four defects. Similarly, the SO_2 concentrations also present a “linear-saturated” growth trend with time under the four defects because of the growth trend of SOF_2 concentrations and the consumption condition of H_2O in the chamber.

3.3. Formation Rates of SF_6 Decomposed Components

The severity of the insulation defect is difficult to assess accurately based only on the concentrations of SF_6 decomposed components. The formation rates of SF_6 decomposed components should also be considered because they can directly reflect the fault consumed energy, fault type, fault severity, and fault development process. Therefore, this study adopts the effective formation rate (R_{RMS}) [47] to study the relationship between SF_6 decomposed components and PD types. R_{RMS} is expressed as follows:

$$R_{RMS} = \sqrt{\frac{\sum_{j=1}^4 R_{aij}^2}{4}}, \quad (2)$$

where R_{aij} is the absolute formation rate of component i in day j . R_a is the absolute formation rate (ppm/day) and is calculated using the following equation:

$$R_a = \frac{C_{i2} - C_{i1}}{\Delta t}, \quad (3)$$

where C_{i1} is the concentration of component i from the first measurement time, C_{i2} is the concentration of component i from the second measurement time, Δt is the time interval between two measurement times, and $\Delta t = 1$ day in this study.

The effective formation rates of SF₆ decomposed components under the four defects are shown in Table 3. Under the protrusion defect, the R_{RMS} of CF₄ is the smallest, and the effective formation rates of CO₂, SO₂F₂, SOF₂, and SO₂ are remarkably larger than those under the other three defects. The R_{RMS} of SOF₂ under the particle defect is three times the R_{RMS} of SOF₂ under the pollution defect, which is eight times the R_{RMS} of SOF₂ under the gap defect. The R_{RMS} of CO₂ under the pollution defect is nearly two times the effective formation rates of CO₂ under the particle and gap defects. Under the gap defect, the sum of the effective formation rates of SF₆ decomposed components is the smallest. The effective formation rates of SF₆ decomposed components under the four defects are different from one another, thus, they can be used to recognize the PD types.

Table 3. Effective formation rates of SF₆ decomposed components.

Defect Type	R_{RMS} (ppm/day)				
	CF ₄	CO ₂	SO ₂ F ₂	SOF ₂	SO ₂
Protrusion	0.04	5.59	18.79	79.96	1.95
Particle	0.68	1.53	1.66	10.00	1.25
Pollution	0.05	2.76	1.02	3.50	0.33
Gap	0.09	1.26	0.44	1.31	0.10

Under the particle defect, the aluminum balls (Weihua Aluminum Industry Co., Ltd., Wuhan, China, mass fraction of C element: 0.88%) can provide C atoms for CF₄ formation, and the PD has the second largest N , Q_{avg} , and Q_{sec} , thus, the R_{RMS} of CF₄ is the largest. Under the pollution defect, the epoxy block can provide abundant C atoms for CO₂ formation, thus, the R_{RMS} of CO₂ is larger than that under the particle defect. Under the protrusion, pollution, and gap defects, the R_{RMS} relationship of CO₂ is consistent with the value relationships of N and Q_{sec} . Therefore, the R_{RMS} of CO₂ is determined by the following two aspects: (1) the N and Q_{sec} of PD; (2) whether an organic insulating material is present near the PD area. Under the four defects, the R_{RMS} relationships of SO₂F₂, SOF₂, and SO₂ are consistent with the value relationships of N and Q_{sec} . Thus, the N and Q_{sec} of PD are the main factors that influence the effective formation rates of SO₂F₂, SOF₂, and SO₂.

3.4. Concentration Ratios of SF₆ Decomposed Components

The gas chamber volume and trace H₂O and O₂ affect the concentrations and formation rates of SF₆ decomposed components. Based on the three-ratio method in oil chromatographic analysis, $C(\text{SOF}_2)/C(\text{SO}_2\text{F}_2)$, $C(\text{CF}_4)/C(\text{CO}_2)$, and $C(\text{SO}_2\text{F}_2 + \text{SOF}_2)/C(\text{CF}_4 + \text{CO}_2)$ were selected as characteristic quantities to recognize the PD types [21,22]. These three concentration ratios have definite physical meaning. $C(\text{SOF}_2)/C(\text{SO}_2\text{F}_2)$ is used to describe PD severity; $C(\text{CF}_4)/C(\text{CO}_2)$ is used to describe the structure of insulation defect; $C(\text{SO}_2\text{F}_2 + \text{SOF}_2)/C(\text{CF}_4 + \text{CO}_2)$ is used to describe the deterioration degree of carbonaceous material (the metal part and organic insulation). In [21,22], the formation characteristics of SO₂ were not studied because of the limitations of the experimental conditions. SOF₂ is prone to hydrolysis in producing SO₂. Currently, the common electrochemical sensors can respond to SOF₂ and SO₂ in the field overhaul. IEC 60480:2004 [48] stipulates that the sum of the concentrations of SOF₂ and SO₂ in the SF₆ gas that can be recycled cannot exceed 12 ppm. Thus, SO₂ is an important component and can be selected as a characteristic gas for field detection. Based on the experimental data in this study, $C(\text{SOF}_2 + \text{SO}_2)/C(\text{SO}_2\text{F}_2)$, $\ln(C(\text{CO}_2)/C(\text{CF}_4))$, and $C(\text{SO}_2\text{F}_2 + \text{SOF}_2 + \text{SO}_2)/C(\text{CF}_4 + \text{CO}_2)$ are selected as characteristic quantities to study the relationship between the decomposition characteristics of SF₆ and PD types.

The value relationship of $C(\text{SOF}_2 + \text{SO}_2)/C(\text{SO}_2\text{F}_2)$ under the four defects is: particle defect > protrusion defect > pollution defect > gap defect (Figure 8a). A smaller value of $C(\text{SOF}_2 + \text{SO}_2)/C(\text{SO}_2\text{F}_2)$

indicates a larger PD energy and a more serious fault. Therefore, the PD energy under the particle defect is the smallest, and the PD energies under the other three defects are close to one another. The curves in Figure 8b can be easily distinguished from one another, the curves have no intersection, indicating significant differences among the structures of the four defects. Thus, $\ln(C(\text{CO}_2)/C(\text{CF}_4))$ can be used to recognize the four defects in this study.

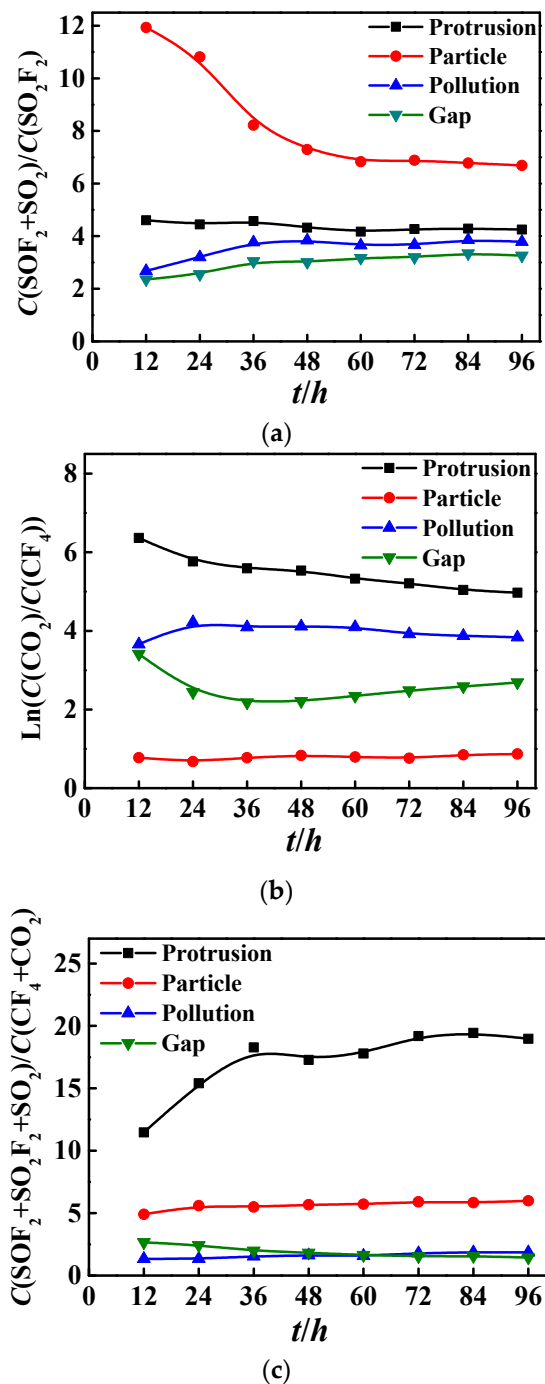


Figure 8. Change curves of the concentration ratios of SF₆ decomposed components with time: (a) $C(\text{SOF}_2) / C(\text{SO}_2\text{F}_2)$; (b) $\ln(C(\text{CO}_2) / C(\text{CF}_4))$; and (c) $C(\text{SOF}_2 + \text{SO}_2\text{F}_2 + \text{SO}_2) / C(\text{CF}_4 + \text{CO}_2)$.

A smaller value of $C(\text{SO}_2\text{F}_2 + \text{SOF}_2 + \text{SO}_2)/C(\text{CF}_4 + \text{CO}_2)$ indicates a more serious deterioration of the carbonaceous materials. Therefore, the deteriorations of the carbonaceous materials under the pollution and gap defects are the most serious, and that under the protrusion defect is the lightest.

If the concentration ratios of the SF_6 decomposed components are to be used in recognizing the PD types in the field fault diagnosis, then the selected ratios cannot present significant fluctuations with time. Even if insulation defects exist in GIE, the concentrations of SF_6 decomposed components have been basically stable after a long period of operation, thus, the concentration ratios are unlikely to appear as large fluctuations with time. As shown in Figure 8, the values of $C(\text{SOF}_2 + \text{SO}_2)/C(\text{SO}_2\text{F}_2)$, $\text{Ln}(C(\text{CO}_2)/C(\text{CF}_4))$, and $C(\text{SO}_2\text{F}_2 + \text{SOF}_2 + \text{SO}_2)/C(\text{CF}_4 + \text{CO}_2)$ are basically stable after 36 h. The change curves of $C(\text{SO}_2\text{F}_2 + \text{SOF}_2 + \text{SO}_2)/C(\text{CF}_4 + \text{CO}_2)$ under the pollution and gap defects are close, whereas the other curves can be easily distinguished from one another. Therefore, $C(\text{SOF}_2 + \text{SO}_2)/C(\text{SO}_2\text{F}_2)$, $\text{Ln}(C(\text{CO}_2)/C(\text{CF}_4))$, and $C(\text{SO}_2\text{F}_2 + \text{SOF}_2 + \text{SO}_2)/C(\text{CF}_4 + \text{CO}_2)$ can be used to recognize the PD types.

4. PD Recognition

This study uses the back propagation (BP) neural network algorithm [29–38] to recognize the PD types. The concentrations and concentration ratios of SF_6 decomposed components are selected as the input matrix of the network. Then the recognition results are analyzed, and the best characteristic quantity for PD recognition is extracted.

BP neural network is a multi-layer feedforward network, which uses the steepest descent method to achieve the minimum of mean square error between the expected output and actual output. The structure of BP neural network is shown in Figure 9, including the input, hidden, and output layers. The learning process of BP neural network is composed of the forward propagation (FP) of signal and the BP of error. In the FP process, the input signals are transferred from the input layer to the hidden layer until the output layer. If the output layer does not obtain an expected output, then the weights and thresholds should be adjusted to reduce the predicted error in the BP process.

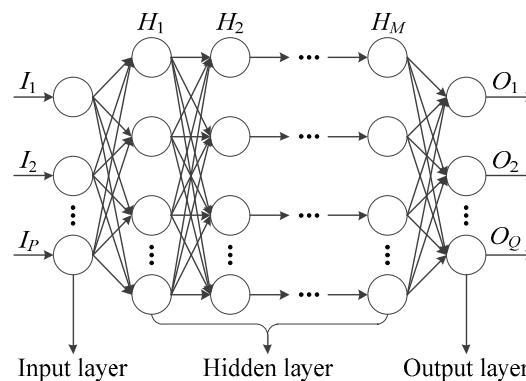


Figure 9. Structure of BP neural network.

Step 1: Set the variables and parameters. As shown in Figure 8, the values of $C(\text{SOF}_2 + \text{SO}_2)/C(\text{SO}_2\text{F}_2)$, $\text{Ln}(C(\text{CO}_2)/C(\text{CF}_4))$, and $C(\text{SO}_2\text{F}_2 + \text{SOF}_2 + \text{SO}_2)/C(\text{CF}_4 + \text{CO}_2)$ are basically stable after 36 h. The experimental data of these three concentration ratios after 36 h are selected as the input matrix of the network, namely, $I_k = [c(\text{SOF}_2 + \text{SO}_2)/c(\text{SO}_2\text{F}_2), \text{Ln}(c(\text{CO}_2)/c(\text{CF}_4)), c(\text{SOF}_2 + \text{SO}_2\text{F}_2 + \text{SO}_2)/c(\text{CF}_4 + \text{CO}_2)]_k$, where $k = 1, 2, \dots, 24$, as shown in Table 4. The protrusion, particle, pollution, and gap defects are encoded as the network output. The output matrix (T) is shown in Table 5.

Step 2: Initialize the network. Random numbers in the range of [0, 1] are assigned to the connection weights and the thresholds. Set the maximum number of iterations is 100, the learning rate is 0.1, the permissible error between expected output and actual output is 0.01, and the number of the hidden layers is 10.

Step 3: Input the training samples. The 75% (18 groups) of the above 24 groups of experimental data are randomly extracted as the training samples, and the remaining 25% data (6 groups) are used as the test samples. The training samples are used to train the BP neural network model. Then, the trained model is used to recognize the test samples.

Step 4: Train BP neural network and recognize PD types. To make the recognition results statistically significant, Step 3 is repeated 100 times. Thus, the number of the test samples is 600. The trained BP neural network models are used to recognize these 600 groups of test samples, the recognition results are shown in Table 6. Therefore, the concentration ratios of SF₆ decomposed components are used to recognize the PD types, the total recognition accuracy rate is: (169 + 132 + 114 + 109)/600 ≈ 87%.

Table 4. Input matrix of BP neural network.

PD Type	<i>k</i>	<i>t/h</i>	$C(\text{SOF}_2 + \text{SO}_2)/C(\text{SO}_2\text{F}_2)$	$\text{Ln}(C(\text{CO}_2)/C(\text{CF}_4))$	$C(\text{SO}_2\text{F}_2 + \text{SOF}_2 + \text{SO}_2)/C(\text{CF}_4 + \text{CO}_2)$
Protrusion	1	36	4.57	5.59	18.28
	2	48	4.33	5.53	17.27
	3	60	4.17	5.33	17.79
	4	72	4.27	5.21	19.19
	5	84	4.29	5.04	19.44
	6	96	4.25	4.97	18.97
Particle	7	36	8.22	0.78	5.49
	8	48	7.29	0.83	5.67
	9	60	6.83	0.79	5.72
	10	72	6.89	0.76	5.90
	11	84	6.78	0.85	5.84
	12	96	6.69	0.87	5.98
Pollution	13	36	3.77	4.09	1.53
	14	48	3.84	4.12	1.62
	15	60	3.65	4.10	1.57
	16	72	3.67	3.92	1.79
	17	84	3.86	3.88	1.86
	18	96	3.79	3.84	1.86
Gap	19	36	3.05	2.18	1.99
	20	48	3.01	2.21	1.82
	21	60	3.17	2.35	1.64
	22	72	3.20	2.48	1.54
	23	84	3.35	2.59	1.55
	24	96	3.26	2.69	1.44

Table 5. Output matrix of BP neural network.

Number	Output Matrix (T)	PD Type
1	[0, 0, 0, 1]	Protrusion
2	[0, 0, 1, 0]	Particle
3	[0, 1, 0, 0]	Pollution
4	[1, 0, 0, 0]	Gap

Table 6. Recognition result using the concentration ratios of SF₆ decomposed components as the input matrix.

Item	PD Type				Total
	Protrusion	Particle	Pollution	Gap	
Sample number	169	141	138	152	600
Accuracy number	169	132	114	109	524
Accuracy rate	100%	93.62%	82.61%	71.71%	87.33%

Similarly, the concentrations of SF₆ decomposed components are selected as the input matrix of the network. From the previous analysis, CF₄ concentration is not suitable as a characteristic quantity to recognize the PD types. Thus, the input matrix is $I_k = [c(\text{CO}_2), c(\text{SO}_2\text{F}_2), c(\text{SO}_2\text{F}_2), c(\text{SO}_2)]_k$, where

$k = 1, 2, \dots, 32$. The output matrix remains unchanged (Table 5). Steps 2–4 are conducted, and the recognition results are shown in Table 7. Therefore, the concentrations of SF₆ decomposed components are used to recognize PD types, the total recognition accuracy rate is: $(167 + 165 + 105 + 104)/800 \approx 68\%$.

Table 7. Recognition result using the concentrations of SF₆ decomposed components as the input matrix.

Item	PD Type				Total
	Protrusion	Particle	Pollution	Gap	
Sample number	176	216	187	221	800
Accuracy number	167	165	105	104	541
Accuracy rate	94.89%	76.39%	56.15%	47.06%	67.63%

Evidently, the total accuracy rate of PD recognition by using the concentration ratios is nearly 20% higher than that by using the concentrations. Moreover, $c(\text{SOF}_2 + \text{SO}_2)/c(\text{SO}_2\text{F}_2)$, $\text{Ln}(c(\text{CO}_2)/c(\text{CF}_4))$, and $c(\text{SOF}_2 + \text{SO}_2\text{F}_2 + \text{SO}_2)/c(\text{CF}_4 + \text{CO}_2)$ have definite physical meaning. Therefore, these three concentration ratios are more suitable as the characteristic quantities for PD recognition than the concentrations of SF₆ decomposed components.

To test the recognition performance of BP neural network, the 24 groups of concentration ratios data in this study are selected to train the network model. Then, the trained model is used to recognize another 24 groups of concentration ratio data produced by the same experiment. These 24 groups of data are also basically stable. The deviations of the concentrations of SF₆ decomposed components between these two experiments are less than 10%. The confusion matrix of the recognition result is shown in Table 8, the total recognition accuracy rate is 87.5%, and a good recognition effect is obtained.

Table 8. Confusion matrix of the recognition result.

Real PD Type	Number of Samples in Each PD Type in the Recognition Result			
	Protrusion	Particle	Pollution	Gap
Protrusion	6	0	0	0
Particle	0	6	0	0
Pollution	0	0	5	1
Gap	0	0	2	4

5. Discussion

This research studied the decomposition characteristics of SF₆ under negative DC-PD, and used BP neural network algorithm to recognize four typical insulation faults in DC-GIE. This study could lay a solid foundation of using GCA method to diagnose the insulation faults in DC-GIE and assess its insulation status. However, the concentrations of SF₆ decomposed components are not only related to PD type, they are also affected by PD strength [49], the H₂O [50], O₂ [51], and absorbent [52] in DC-GIE, and so on. This study did not consider these impact factors. To achieve better performance in using GCA method for PD recognition, the influence of these factors on the concentrations of SF₆ decomposed components must be studied. Moreover, this study used the decomposition characteristics of SF₆ to recognize the four common PD types in DC-GIE, and obtained a good recognition effect in the laboratory. We should focus on the research of the field application in the future, and use the engineering data to verify the validity of the method in this study and make corresponding improvements to this method.

6. Conclusions

The decomposition characteristics of SF₆ under four types of negative DC partial discharges are obtained in this study. The relationship between the decomposition characteristics of SF₆ and the PD

types was further studied. Moreover, BP neural network algorithm is used to recognize the PD types. The following conclusions can be drawn from this study:

- The negative DC partial discharges caused by the four defects decompose the SF₆ gas and generate five stable decomposed components, namely, CF₄, CO₂, SO₂F₂, SOF₂, and SO₂. A close relationship exists between the decomposition characteristics of SF₆ and the types of insulation defects. The decomposition characteristics of SF₆ can be used to diagnose the type and severity of insulation fault in DC-GIE.
- BP neural network algorithm is used to recognize the PD types. The recognition results show that the total recognition accuracy rate is 67.63% and 87.33% when the concentrations and concentration ratios of SF₆ decomposed components are selected as the input matrix of the network, respectively. Therefore, the concentration ratios of SF₆ decomposed components are more suitable as the characteristic quantities for PD recognition than the concentrations of those.
- $C(\text{SOF}_2 + \text{SO}_2)/C(\text{SO}_2\text{F}_2)$, $\text{Ln}(C(\text{CO}_2)/C(\text{CF}_4))$, and $C(\text{SO}_2\text{F}_2 + \text{SOF}_2 + \text{SO}_2)/C(\text{CF}_4 + \text{CO}_2)$ are used to recognize the PD types. The 24 groups of concentration ratio data in this study are selected to train the BP neural network model. Then, the trained model is used to recognize another 24 groups of concentration ratio data produced by the same experiment. The total recognition accuracy rate is 87.5%, and a good recognition effect is obtained.

Acknowledgments: All the research work has been funded by the National Natural Science Foundation of China (Grant No. 51537009 and 51607127) and China Postdoctoral Science Foundation (Grant No. 2016T90723). We sincerely express our thankfulness here.

Author Contributions: Ju Tang and Fuping Zeng conceived and designed the experiments; Xu Yang, Gaoxiang Ye, Qiang Yao, and Yulong Miao performed the experiments; Xu Yang and Fuping Zeng analyzed the data; Ju Tang and Xu Yang wrote the paper.

Conflicts of Interest: The authors declare no conflict of interest.

References

1. Ohki, Y. Thyristor valves and GIS in Kii channel HVDC link. *IEEE Electr. Insul. Mag.* **2001**, *17*, 78–79. [[CrossRef](#)]
2. Hasegawa, T.; Yamaji, K.; Hatano, M. Development of insulation structure and enhancement of insulation reliability of 500 kV DC GIS. *IEEE Trans. Power Deliv.* **1997**, *12*, 192–202. [[CrossRef](#)]
3. Hasegawa, T.; Yamaji, K.; Hatano, M. DC dielectric characteristics and conception of insulation design for DC GIS. *IEEE Trans. Power Deliv.* **1996**, *11*, 1776–1782. [[CrossRef](#)]
4. Menju, S.; Takahashi, K. DC dielectric strength of a SF₆ gas insulated system. *IEEE Trans. Power Deliv.* **1978**, *97*, 217–224. [[CrossRef](#)]
5. Evgeni, K.V. HVDC gas insulated apparatus: Electric field specificity and insulation design concept. *IEEE Electr. Insul. Mag.* **2002**, *18*, 7–14.
6. Mendik, M.; Lowder, S.M.; Elliott, F. Long term performance verification of high voltage DC GIS. In Proceedings of the 1999 IEEE Transmission and Distribution Conference, New Orleans, LA, USA, 11–16 April 1999; pp. 484–488.
7. Beyer, C.; Jenett, H.; Kfocow, D. Influence of reactive SF_x gases on electrode surfaces after electrical discharges under SF₆ atmosphere. *IEEE Trans. Dielectr. Electr. Insul.* **2000**, *7*, 234–240. [[CrossRef](#)]
8. Chu, F.Y. SF₆ decomposition in gas-insulated equipment. *IEEE Trans. Dielectr. Electr. Insul.* **1986**, *21*, 693–725. [[CrossRef](#)]
9. Van Brunt, R.J.; Herron, J.T. Fundamental processes of SF₆ decomposition and oxidation in glow and corona discharges. *IEEE Trans. Dielectr. Electr. Insul.* **1990**, *25*, 75–94. [[CrossRef](#)]
10. Chang, C.; Chang, C.S.; Jin, J.; Hoshino, T.; Hanai, M.; Kobayashi, N. Source classification of partial discharge for gas insulated substation using wave shape pattern recognition. *IEEE Trans. Dielectr. Electr. Insul.* **2005**, *12*, 374–386. [[CrossRef](#)]
11. Dreisbusch, K.; Kranz, H.G.; Schnettler, A. Determination of a failure probability prognosis based on PD-diagnostics in GIS. *IEEE Trans. Dielectr. Electr. Insul.* **2008**, *15*, 1707–1714. [[CrossRef](#)]
12. Istad, M.; Runde, M. Thirty-six years of service experience with a national population of gas-insulated substations. *IEEE Trans. Power Deliv.* **2010**, *25*, 2448–2454. [[CrossRef](#)]

13. Van Brunt, R.J. Production rates for oxy-fluorides SOF_2 , SO_2F_2 and SOF_4 in SF_6 corona discharges. *J. Res. Natl. Bur. Stand.* **1985**, *90*, 229–253. [[CrossRef](#)]
14. Piemontesi, M.; Niemeyer, L. Sorption of SF_6 and SF_6 decomposition products by activated alumina and molecular sieve 13X. In Proceedings of the 1996 IEEE International Symposium on Electrical Insulation, Montreal, QC, Canada, 16–19 June 1996; pp. 828–838.
15. Van Brunt, R.J.; Herron, J.T. Plasma chemical model for decomposition of SF_6 in a negative glow corona discharge. *Phys. Scr.* **1994**, *53*, 9–29. [[CrossRef](#)]
16. Prakash, K.S.; Srivastava, K.D.; Morcos, M.M. Movement of particles in compressed SF_6 GIS with dielectric coated enclosure. *IEEE Trans. Dielectr. Electr. Insul.* **1997**, *4*, 344–347. [[CrossRef](#)]
17. Casanovas, A.M.; Casanovas, J.; Lagarde, F. Study of the decomposition of SF_6 under dc negative polarity corona discharges (point-to-plane geometry): Influence of the metal constituting the plane electrode. *J. Appl. Phys.* **1992**, *72*, 3344–3354. [[CrossRef](#)]
18. Belmadani, B.; Casanovas, B.; Casanovas, A.M. SF_6 decomposition under power arcs: Chemical aspects. *IEEE Trans. Dielectr. Electr. Insul.* **1992**, *26*, 1177–1182. [[CrossRef](#)]
19. Sauers, I.; Ellis, H.W.; Christophorou, L.G. Neutral decomposition products in spark breakdown of SF_6 . *IEEE Trans. Dielectr. Electr. Insul.* **1986**, *21*, 111–120. [[CrossRef](#)]
20. Tang, J.; Li, T.; Hu, Z.; Xiao, B.; Zhang, X.X. Analysis of SF_6 gaseous decomposition components under two kinds of PD defects. *High Volt. Eng.* **2009**, *35*, 487–492.
21. Tang, J.; Liu, F.; Zhang, X.X.; Meng, Q.H.; Zhou, J.B. Partial discharge recognition through an analysis of SF_6 decomposition products part 1: Decomposition characteristics of SF_6 under four different partial discharges. *IEEE Trans. Dielectr. Electr. Insul.* **2012**, *19*, 29–36. [[CrossRef](#)]
22. Tang, J.; Liu, F.; Meng, Q.H.; Zhang, X.X.; Tao, J.G. Partial discharge recognition through an analysis of SF_6 decomposition products part 2: Feature extraction and decision tree-based pattern recognition. *IEEE Trans. Dielectr. Electr. Insul.* **2012**, *19*, 37–44. [[CrossRef](#)]
23. Dourdour, A. Study of the decomposition of wet SF_6 , subjected to 50-Hz ac corona discharges. *J. Appl. Phys.* **1989**, *65*, 1852–1857. [[CrossRef](#)]
24. Belarbi, A.; Pradayrol, C.; Casanovas, J.; Casanovas, A.M. Influence of discharge production conditions, gas pressure, current intensity and voltage type on SF_6 dissociation under point-plane corona discharges. *J. Appl. Phys.* **1995**, *77*, 1398–1406. [[CrossRef](#)]
25. Chen, C.L.; Chantry, P.J. Photo-enhanced dissociative electron attachment in SF_6 and its isotopic selectivity. *J. Chem. Phys.* **1979**, *71*, 38–97. [[CrossRef](#)]
26. Dincer, M.S.; Raju, G.R. Monte Carlo simulation of the motion of electrons in SF_6 in uniform electric field. *J. Appl. Phys.* **1983**, *54*, 6311–6316. [[CrossRef](#)]
27. Sauers, I.; Adcock, J.L.; Christophorou, L.G. Gas phase hydrolysis of sulfur tetrafluoride. *J. Chem. Phys.* **1985**, *83*, 2618–2619. [[CrossRef](#)]
28. Boggs, S.A.; Stone, C. Fundamental limitations in the measurement of corona and partial discharge. *IEEE Trans. Dielectr. Electr. Insul.* **1982**, *17*, 143–150. [[CrossRef](#)]
29. Fanni, A.; Giua, A.; Sandoli, E. Neural networks for multiple fault diagnosis in analog circuits. In Proceedings of the 1993 IEEE International Workshop on Defect and Fault Tolerance in VLSI systems, Venice, Italy, 27–29 October 1993; pp. 303–310.
30. Kirkland, L.V.; Wright, R.G. Using neural networks to solve testing problems. *IEEE Aerosp. Electron. Syst. Mag.* **1996**, *12*, 36–40. [[CrossRef](#)]
31. Aminian, M.; Aminian, F. Neural-network based analog-circuit fault diagnosis using wavelet transform as preprocessor. *IEEE Trans. Circuits Syst. II Analog Digit. Signal Process.* **2000**, *47*, 151–156. [[CrossRef](#)]
32. Karnin, E.D. A simple procedure for punning back-propagation trained neural networks. *IEEE Trans. Neural Netw.* **1990**, *1*, 239–242. [[CrossRef](#)] [[PubMed](#)]
33. Mas'ud, A.A.; Albarracín, R.; Ardila-Rey, J.A.; Muhammad-Sukki, F.; Illias, H.A.; Bani, N.A.; Munir, A.B. Artificial neural network application for partial discharge recognition: Survey and future directions. *Energies* **2016**, *9*, 574. [[CrossRef](#)]
34. Khan, Y. Partial discharge pattern analysis using PCA and back-propagation artificial neural network for the estimation of size and position of metallic particle adhering to spacer in GIS. *Electr. Eng.* **2016**, *98*, 29–42. [[CrossRef](#)]

35. Majidi, M.; Fadali, M.S.; Etezadi-Amoli, M.; Oskuoee, M. Partial discharge pattern recognition via sparse representation and ANN. *IEEE Trans. Dielectr. Electr. Insul.* **2015**, *22*, 1061–1070. [[CrossRef](#)]
36. Gulski, E.; Krivda, A. Neural networks as a tool for recognition of partial discharges. *IEEE Trans. Dielectr. Electr. Insul.* **1993**, *28*, 984–1001. [[CrossRef](#)]
37. Satish, L.; Zaengl, W.S. Artificial neural networks for recognition of 3-D partial discharge patterns. *IEEE Trans. Dielectr. Electr. Insul.* **1994**, *1*, 265–275. [[CrossRef](#)]
38. Hozumi, N.; Okamoto, T.; Imajo, T. Discrimination of partial discharge patterns using a neural network. *IEEE Trans. Dielectr. Electr. Insul.* **1992**, *27*, 550–556. [[CrossRef](#)]
39. Ding, W.D.; Zhou, W.W.; Ren, X. Decomposition characteristics of SF₆ under partial discharges with point-to-plane electrode defect. *IEEE Trans. Dielectr. Electr. Insul.* **2013**, *20*, 1727–1736.
40. Okabe, S.; Yamagiwa, T.; Okubo, H. Detection of harmful metallic particles inside gas insulated switchgear using UHF sensor. *IEEE Trans. Dielectr. Electr. Insul.* **2008**, *15*, 701–709. [[CrossRef](#)]
41. Ren, M.; Zhang, C.X.; Dong, M. Partial discharges triggered by metal-particle on insulator surface under standard oscillating impulses in SF₆ gas. *IEEE Trans. Dielectr. Electr. Insul.* **2015**, *22*, 3007–3018. [[CrossRef](#)]
42. Tang, J.; Ren, X.L.; Zhang, X.X.; Liu, F. Decomposition characteristics of SF₆ under different partial discharge strengths caused by defected insulation in air gap. *Power Syst. Technol.* **2012**, *36*, 40–45.
43. DL/T 596–1996 Preventive Test Code for Electric Power Equipment. Available online: <http://www.doc88.com/p-9763610841190.html> (accessed on 12 April 2017).
44. IEC 60270:2000 High-voltage Test Techniques—Partial Discharge Measurements. Available online: <http://www.doc88.com/p-868119919771.html> (accessed on 12 April 2017).
45. Auger, P.; Poggiale, J.C. Emergence of population growth models: Fast migration and slow growth. *J. Theor. Biol.* **1996**, *182*, 99–108. [[CrossRef](#)] [[PubMed](#)]
46. Sibly, R.M.; Barker, D.; Denham, M.C.; Home, J.; Pagel, M. On the regulation of populations of mammals, birds, fish and insects. *Ecol. Lett.* **2005**, *309*, 607–610. [[CrossRef](#)] [[PubMed](#)]
47. Tang, J.; Zeng, F.P.; Pan, J.Y.; Zhang, X.X.; Yao, Q. Correlation analysis between formation process of SF₆ decomposed components and partial discharge qualities. *IEEE Trans. Dielectr. Electr. Insul.* **2013**, *20*, 864–875. [[CrossRef](#)]
48. IEC 60480:2004 Guidelines for the Checking and Treatment of Sulfur Hexafluoride (SF₆) Taken from Electrical Equipment and Specification for Its Re-Use. Available online: <http://pan.baidu.com/share/link?shareid=3125702881&uk=3894130273> (accessed on 12 April 2017).
49. Tang, J.; Pan, J.Y.; Zhang, X.X.; Zeng, F.P.; Yao, Q.; Hou, X.Z. Correlation analysis between SF₆ decomposed components and charge magnitude of partial discharges initiated by free metal particles. *IET Sci. Meas. Technol.* **2014**, *8*, 170–177. [[CrossRef](#)]
50. Zeng, F.P.; Tang, J.; Zhang, X.X.; Pan, J.Y. Influence regularity of trace H₂O on SF₆ decomposition characteristics under partial discharge of needle-plate electrode. *IEEE Trans. Dielectr. Electr. Insul.* **2015**, *22*, 287–295. [[CrossRef](#)]
51. Tang, J.; Zeng, F.P.; Zhang, X.X.; Pan, J.Y.; Qiu, Y.J. Influence regularity of trace O₂ on SF₆ decomposition characteristics and its mathematical amendment under partial discharge. *IEEE Trans. Dielectr. Electr. Insul.* **2014**, *21*, 105–115. [[CrossRef](#)]
52. Tang, J.; Zeng, F.P.; Liang, X. Study on the influence of adsorbent on SF₆ decomposition characteristics under partial discharge. *Proc. Chin. Soc. Electr. Eng.* **2014**, *34*, 486–494.

